

Evaluation of split-window and dual-angle correction methods for land surface temperature retrieval from Envisat/AATSR data

César Coll, Vicente Caselles, Joan M. Galve, Enric Valor, Raquel Niclòs, and Juan M. Sánchez
Department of Earth Physics and Thermodynamics, Faculty of Physics, University of Valencia.
50, Dr. Moliner. 46100 Burjassot, SPAIN.
Email: cesar.coll@uv.es

Abstract

Land surface temperature (LST) can be derived from thermal infrared remote sensing data provided that atmospheric and emissivity effects are corrected for. In this paper, two correction methods were evaluated using a database of ground LST measurements and concurrent Envisat/Advanced Along Track Scanning Radiometer (AATSR) data. They were the split-window (SW) method, which uses two channels at 11 and 12 μm , and the dual-angle (DA) method using one single channel (11 μm) at two observation angles (close to nadir and around 55° forward). The ground LST measurements were performed in a large, flat and thermally homogeneous area of rice fields during the summers of 2002-2005, when the crop showed full vegetation cover. A total of 23 concurrences of ground measurements and AATSR data were obtained. Results showed that the SW algorithms worked satisfactorily provided that the characteristics of the area are correctly prescribed, either through the classification of the land cover type and vegetation cover fraction, or with the surface emissivity. In this case, the AATSR derived LSTs agreed with the ground LSTs within ± 1.0 °C for all the data of the comparison, with negligible average bias and standard deviation of 0.5 °C. The DA algorithms were less accurate than the SW algorithms for the data used in this study, yielding standard deviations of 1.0 °C.

1. Introduction

The use of thermal infrared remote sensing data is the unique way for the derivation of the land surface temperature (LST) over large portions of the Earth. LSTs are required for the estimation of energy and water fluxes between the atmosphere and the land surface, thus being of great interest for meteorological and climatological studies. The main difficulties in retrieving the LST from satellite data are the correction for the atmospheric effects, mostly the water vapor absorption and emission, and the uncertainty of the surface emissivity, which can be significantly lower than unity and highly variable for land surfaces. Several techniques were proposed in the last years for the correction of thermal infrared satellite data and thus the retrieval of LST. Back in the 70's, methods based on the differential absorption principle [McMillin, 1975] were used for the retrieval of the sea surface temperature (SST). Such methods make use of measurements of the same surface target at different conditions of observation, and they are probably the simplest and operationally feasible approaches for the atmospheric correction of thermal infrared data.

Examples are the split-window (SW) method that uses two channels within the 10.5-12.5 μm atmospheric window [Prabhakara *et al.*, 1974; Deschamps and Phulpin, 1980] or the dual-angle (DA) method using one single channel at two different observation angles [Saunders, 1970]. Algorithms for both techniques usually express the SST as a linear combination of the brightness temperatures in the considered channels or observation angles, with constant coefficients having regional or global validity. The main advantage of these methods is that they do not require an accurate description of the atmosphere (in the form of vertical profiles of temperature and water vapor, ideally obtained from local, concurrent radiosonde data) nor radiative transfer calculations based on these profiles.

More recently, the SW technique was extended to land surfaces by accounting for the effects of surface emissivity [e.g., Becker and Li, 1990; Wan and Dozier, 1996; Coll and Caselles, 1997]. LST algorithms explicitly include a dependence on the surface emissivity in the channels considered, or alternatively different coefficient sets are provided for each land cover type. In any case, the characteristics of the surface must be well known (via the emissivity, or the class and amount of vegetation cover) in order to obtain the LST, which is the main drawback of the method. For this reason, SW methods are expected to work better for near gray-body surfaces with known emissivities (i.e., water and vegetation). The extension of the DA technique to land surfaces requires the knowledge of the surface emissivity at the two observation angles considered. Although it is

generally accepted that the emissivity decreases with the observation angle, little is known about the angular behavior of the land surface emissivity. As a consequence of the anisotropy of the radiation emitted by rough, heterogeneous, non-isothermal surfaces, the DA methods are more difficult to apply for LST retrieval than the SW methods [Caselles *et al.*, 1997].

The validation of satellite derived LSTs with ground measurements is a challenging problem because of the heterogeneity of land surfaces both in temperature and emissivity. Only few LST validation studies can be found in the literature [e. g., Prata, 1994; Wan *et al.*, 2002; Coll *et al.*, 2005]. The comparison between ground, point measurements and satellite, area-averaged measurements is only possible for certain land surfaces that are thermally homogeneous at various spatial scales, from the footprint of ground instruments to several satellite pixels. Such areas exist, the most suitable being densely vegetated surfaces and bare surfaces or deserts.

A database of ground measurements of LST was collected in a test site close to Valencia, Spain concurrently to Envisat/Advanced Along Track Scanning Radiometer (AATSR) overpasses, with the aim of evaluating SW and DA correction methods for LST retrieval. The AATSR [Llewellyn-Jones *et al.*, 2001] has seven bands at 0.55, 0.66, 0.87, 1.6, 3.7, 11 and 12 μm . It uses a conical scanning mechanism which allows the observation of the same target with two different viewing angles, first at an angle of around 55° (the forward view), and 120 s later at an angle close to the vertical (the nadir view; in fact from 0° to 23.5°). The nominal spatial resolution of AATSR is 1 km \times 1 km for the nadir view and 1.5 km \times 2 km for the forward view. Recently, an operational LST product was included, which is based on the SW method using the nadir view, 11 and 12 μm channels of AATSR [Prata, 2000]. Ground data from the Valencia test site were used by Coll *et al.* [2005] for validating LSTs derived with SW algorithms for Terra/Moderate Resolution Imaging Spectroradiometer (MODIS) and AATSR data. In that paper, we only checked five concurrent ground and AATSR data for 2002, plus eleven MODIS concurrences for 2002-2004. In the present paper we completed the evaluation of AATSR derived LSTs for a total of 23 concurrences in 2002-2005. In addition, we analyzed the performance of the DA method with the same ground LST database.

This paper is organized as follows. Section 2 presents the experimental data used for the evaluation of the AATSR derived LSTs, including the database of ground LSTs, the emissivity measurements, and the AATSR

data. Section 3 shows and discusses the results for the validation of different SW algorithms applicable to AATSR data. Section 4 deals with the validation of DA algorithms. The conclusions are given in section 5.

2. Experimental data

Experimental campaigns were carried out in the Valencia test site during the summers of 2002-2005 with the aim of providing validation data for AATSR derived LSTs. The site is located in a large, marshy plain dedicated to the intensive cultivation of rice in the Mediterranean coast of Spain, close to the city of Valencia. It is part of a network of sites dedicated to the AATSR LST validation. From the end of June to the beginning of September, rice crops are well developed and attain nearly full cover. In these circumstances, the site shows a high thermal homogeneity and is large enough for AATSR validation. The location of the test site is indicated in the AATSR color composite image of Figure 1, where the rice field area appears in red. In this section, the thermal homogeneity of the site is discussed, then the ground measurements are described and listed, and finally the concurrent AATSR brightness temperatures are given.

2.1. Thermal homogeneity of the site

The thermal homogeneity of the test site was assessed using AATSR and Advanced Spaceborne Thermal Emission and Reflection Radiometer (ASTER) data acquired over the area. Figure 2 shows AATSR images of brightness temperatures at 11 μm , (a) nadir view, and (b) forward view, centered at the rice field area. Figure 3 shows a 10 \times 10 km² image of brightness temperature in ASTER band 13 (10.66 μm) at a spatial resolution of 90 m. In these images, a polygon covering approximately the same area around the ground measurement site is shown. We calculated the maximum, minimum, and average brightness temperatures (T_M , T_m , and T_{av} , respectively), and the standard deviation (σ) for the pixels enclosed by the polygon. In the case of AATSR (39 pixels), we obtained $T_M=27.71$ °C, $T_m=26.84$ °C, $T_{av}=27.19$ °C, and $\sigma=0.20$ °C for the nadir view (Figure 2a), and $T_M=25.81$ °C, $T_m=25.12$ °C, $T_{av}=25.42$ °C, and $\sigma=0.19$ °C for the forward view (Figure 2b).

For the ASTER scene (Figure 3), we excluded the pixels within the dashed-line square corresponding to the hot spot at 0°18'50''W, 39°14'30''N (a built-up site), which has the largest temperature heterogeneity in the rice crop area. According to the temperatures and size of the hot spot, it could increase the surface temperature at the 1 km² scale by a maximum of 1 °C with regard to the surrounding rice field temperatures. This effect was sometimes noticeable in the AATSR images, so that the hot pixel could be removed for the comparison with the

ground measurements. For the 4400 pixels (~36 km²) selected, we obtained $T_M=30.15$ °C, $T_m=25.79$ °C, $T_{av}=26.89$ °C, and $\sigma=0.45$ °C. Figure 4 shows a histogram of the ASTER brightness temperatures for the selected pixels. About 97 % of the pixels had temperatures between 26.0 °C and 28.0 °C. The highest temperatures (28.0 – 30.0 °C) were for a few pixels corresponding to narrow tracks and roads that cross the site, as can be observed in Figure 3. The impact of these pixels on the 1 km²-scale surface temperature was negligible. For comparison, the values for an area of 620 pixels (5 km²) at the nearby sea surface were $T_M=24.73$ °C, $T_m=23.89$ °C, $T_{av}=24.24$ °C, and $\sigma=0.18$ °C. The noise equivalent temperature difference of ASTER TIR bands is ≤ 0.3 °C [Yamaguchi *et al.*, 1998]. These results show that the experimental area contains a considerable number of 1 km² pixels for which the variability in surface temperature, as seen in the ASTER data, is about 0.2–0.5 °C. Therefore this site could be used for the validation of AATSR derived LSTs, in both the nadir and the forward views.

2.2. Ground LST measurements

Ground LSTs were measured in the test site by means of up to four thermal infrared radiometers distributed over a square of 1 km² within the rice field area. The instruments were two CIMEL CE 312 radiometers (CE1 and CE2) with four bands (1 to 4 at 8-13 μm , 11.5-12.5 μm , 10.5-11.5 μm and 8.2-9.2 μm , respectively), one Everest model 112.2L thermometer with one single band (8-13 μm) and one AGA model 80 thermometer (single band, 8-13 μm). Bands 2 and 3 of CE 312 are similar to the 12 and 11 μm channels of AATSR, respectively. Each radiometer was assigned to one part of the 1 km² square in order to cover the area as much as possible. In the 2002 and 2003 campaigns, the 1 km² test site was centered at 0°17'50''W, 39°14'27''N. For the 2004 campaign, the test site was moved 1 km North (center at 0°17'43''W, 39°15'01''N), while in 2005 it was moved again to the North (center at 0°18'28''W, 39°15'54'') (see Fig. 3).

Radiometers were carried back and forth along transects of 100 – 200 m looking at the surface at angles close to nadir, during 30 minutes around the satellite overpass. The field of view of the radiometers was about 30 cm on the crop surface. Measurements were made at a rate of more than 5 measurements per minute, covering a distance of 30-50 m per minute. The methodology for the measurement of ground LSTs for comparison with AATSR derived LSTs is described by *Coll et al.* [2005]. Some details are given below:

a) Calibration of the field radiometers. The instruments were calibrated with a blackbody source and intercompared in the field along the campaigns. The absolute accuracies, $\sigma(\text{cal})$, of the CE1 and CE2 radiometers

were ± 0.2 °C and ± 0.1 °C, respectively. The Everest and AGA instruments had lower accuracies and may give biased LST measurements depending on the ambient operating temperature. Using the blackbody measurements and band 1 of the CE2 radiometer as a reference, linear calibration equations were derived for these instruments each day of campaign. The standard error of estimate of the calibration equations was taken as $\sigma(\text{cal})$. For the Everest (AGA), $\sigma(\text{cal})$ was between ± 0.5 and ± 0.7 °C (± 0.7 and ± 0.9 °C).

b) Emissivity correction. Radiometric temperatures were corrected for emissivity effects, including the reflection of the sky radiance. Surface emissivity (ϵ) was measured in the field using the box method [Rubio *et al.*, 2003] for the four channels of the CE 312 radiometers. Results for the rice crops are given in Table 1. These data show high emissivity ($\epsilon > 0.98$) with small spectral variation (< 0.5 %, i. e., comparable to the measurement uncertainties), which is typical for crops with full cover of green vegetation [Salisbury and D'Aria, 1992; Rubio *et al.*, 2003]. The sky radiance L_{sky} was measured along the transects. The error in the emissivity correction is basically due to the uncertainty in the emissivity values used. For an uncertainty of ± 0.5 % in ϵ , the error in temperature due to the emissivity correction, $\sigma(\text{em})$, ranged from ± 0.15 to ± 0.25 °C.

c) Averaging of transect/radiometer ground temperatures. Only the temperatures measured within 3 minutes around the satellite overpass were considered. They were averaged for each transect/radiometer and the standard deviation was calculated. It gives us an estimation of the LST spatial and temporal variability, $\sigma(\text{var})$, in a part of the test site. For the ground data analyzed here, $\sigma(\text{var})$ was typically between ± 0.3 °C and ± 0.5 °C. The total uncertainty in LST for each radiometer, $\sigma(\text{T})$, is given by the combination of the three sources of error (calibration, emissivity correction and variability) according to

$$\sigma(\text{T}) = [\sigma(\text{cal})^2 + \sigma(\text{em})^2 + \sigma(\text{var})^2]^{1/2} \quad (1)$$

For each day of measurement, the ground LST and uncertainty for each radiometer/transect are given in Table 2 together with the date and time of the AATSR overpass. (The data for 29/07/02, which were used in Coll *et al.* [2005], were not considered here due to possible cirrus cloud contamination). The most accurate LSTs correspond to the CE1 and CE2 radiometers, for which the largest source of error was $\sigma(\text{var})$. For the measurement days when the two CE 312 instruments were available, the maximum difference between their measured LSTs was 0.6 °C. In the case of the Everest and AGA instruments, $\sigma(\text{cal})$ was usually the largest source of error. In order to avoid excessive uncertainty due to the calibration problems of the Everest and AGA

instruments, we kept only their LST measurements with $\sigma(T) \leq 1.0$ °C. In addition, we removed the LSTs measured by these instruments that differed by more than 1.0 °C from any of the CE 312 on the same day.

d) Average ground LST. The ground LSTs to be compared with the AATSR derived LSTs were calculated by averaging all the individual ground temperatures within the 3 minute periods for the available radiometers each measurement day. The average LSTs and uncertainties are given in the last column of Table 2. The range of the ground LSTs was roughly from 25 °C to 31 °C, with uncertainties between ± 0.4 °C and ± 0.9 °C. This accuracy interval may be useful for the validation of satellite derived LSTs in real conditions.

2.3. Concurrent AATSR brightness temperatures

For each day of measurements of Table 2, concurrent AATSR scenes were available through the AATSR validation team (University of Leicester) and the European Space Agency (ESA). We identified the pixel closest to the center of the test site in the L1b scenes (geo-referenced, top of the atmosphere data). For the nadir view, we took the 3×3 pixels centered at the closest pixel. This process was done manually and care was taken not to include any pixel that could be partially out of the rice field area, or contain the hot pixel mentioned in section 2.1. For the selected pixels, the average brightness temperature and the standard deviation was calculated for channels at 11 and 12 μm , nadir view (T_{11n} and T_{12n}), as shown in Table 3. The satellite viewing angle for the center pixel was also obtained. For the forward view, due to the larger size of the pixel, we took only the four pixels closest to the center of the test site that were totally within the rice field area. The average temperatures (T_{11f} and T_{12f}) and standard deviation for these pixels are shown in Table 4, together with the satellite viewing angle.

3. VALIDATION OF SPLIT-WINDOW CORRECTION METHODS

In this section, the ground LST – AATSR database is used to evaluate the performance of the SW method for LST retrieval and the accuracy that can be obtained with this technique. These issues were firstly evaluated from an empirical point of view, i. e., by means of linear regression analysis between the ground LST and the AATSR brightness temperatures. Then, different published SW algorithms developed for LST retrieval from AATSR data were validated. First, we checked the AATSR operational algorithm currently implemented to produce the LST product provided in the AATSR L2 data. Second, we checked the quadratic, emissivity dependent algorithm of *Coll and Caselles* [1997], which was adapted to AATSR.

3.1. Linear regression analysis

The basis of SW correction methods relies on the correlation existing between the brightness temperature difference between the two channels, $T_{11n}-T_{12n}$, and the atmospheric and emissivity correction, $LST-T_{11n}$, that must be applied to the brightness temperature in the most transparent channel (T_{11n}) to get the actual LST. In the simplest form, the SW algorithm can be written as

$$LST = T_{11n} + A_{SW}(T_{11n}-T_{12n}) + B_{SW} \quad (2)$$

where A_{SW} and B_{SW} are the split-window coefficients. According to *Coll and Caselles [1997]*, coefficient A_{SW} depends on atmospheric properties and coefficient B_{SW} depends on the emissivity in the channels considered. We analyzed the performance of this simple formulation using the ground LSTs measured in the test site and the corresponding AATSR brightness temperatures. Since the surface conditions of the site remained unchanged during the field campaigns, and the atmospheric conditions were similar, we can regard the SW coefficients as constants. Figure (5) plots the temperature difference $LST-T_{11n}$ against $T_{11n}-T_{12n}$, for which the linear regression yields the SW coefficients A_{SW} and B_{SW} . The results of the regression analysis showed a good coefficient of determination ($R^2=0.82$) and an error of estimate for LST of 0.52 °C for the SW method.

A less constrained linear regression between the ground LST and the brightness temperatures T_{11n} and T_{12n} could be written in the form

$$LST = aT_{11n} + bT_{12n} + c \quad (3)$$

For our data set, the coefficient of determination and the error of estimate for LST were mostly similar ($R^2=0.80$ and 0.51 °C, respectively). Likewise, the SW method could be implemented to the forward view of the 11 and 12 μm channels. Thus, using T_{11f} and T_{12f} (instead of T_{11n} and T_{12n}) in Eq. (3), the linear regression yielded $R^2=0.69$ and error of estimate for LST of 0.64 °C. These results show a worsening of the accuracy of the SW method for large observation angles.

3.2. AATSR LST operational algorithm

The AATSR LST algorithm [*Prata, 2000*] expresses the LST as a linear combination of the nadir brightness temperatures T_{11n} and T_{12n} with coefficients determined by regression over simulated data-sets and depending on

the land cover type (i), the fractional vegetation cover (f), the precipitable water (pw) and the satellite zenith viewing angle (θ):

$$LST = a_{f,i,pw} + b_{f,i}(T_{11n}-T_{12n})^n + (b_{f,i} + c_{f,i})T_{12n} \quad (4)$$

with coefficients given by

$$n = \cos(\theta/5)$$

$$a_{f,i,pw} = 0.4[\sec(\theta)-1]pw + f a_{v,i} + (1-f) a_{s,i}$$

$$b_{f,i} = f b_{v,i} + (1-f) b_{s,i}$$

$$c_{f,i} = f c_{v,i} + (1-f) c_{s,i}$$

These coefficients are provided for 14 different biomes or land cover classes (i=1 to 14). For a given land cover class, two separate sets of coefficients are given for the fully vegetated surface (subscript v) and for the bare surface (subscript s), which are weighted by the fractional vegetation cover f. LST data generated with this algorithm are currently provided as a product with AATSR L2 data. The algorithm is operationally implemented at the Rutherford Appleton Laboratory (RAL) in the so-called RAL processor. The values of i, f and pw are taken from global classification, fractional vegetation cover maps and global climatology at a spatial resolution of 0.5°×0.5° longitude/latitude. Monthly variability is allowed for f and pw. The algorithm is basically linear on the brightness temperatures, since the coefficient n is nearly equal to 1 for the nadir view: for $\theta \leq 23^\circ$, it yields $n \geq 0.997$, for which the LST retrieved for $T_{11n}-T_{12n}=3^\circ\text{C}$ differs by less than 0.03 °C from that retrieved with $n=1$. Moreover, the dependence of LST on the precipitable water is quite small. It appears only in the term $0.4[\sec(\theta)-1]pw$ of coefficient $a_{f,i,pw}$. For $\theta \leq 23^\circ$, the variation of LST is less than 0.04 °C for a variation of 1 cm in pw.

The LST values given by the AATSR LST operational algorithm (RAL processor) for the test site are shown in the fourth column of Table 5. They were extracted from the L2 data for 3×3 pixels centered on the pixel closest to the test site. The seventh column shows the difference between the ground and the AATSR derived LSTs. According to these results, the RAL processor seems to overestimate the ground LSTs by 3.5 °C in average. Thus the standard LST product would be useless at this scale of application. It appears that the 0.5° resolution maps used by the operational algorithm is too coarse in order to properly assign the land cover type (i) and the fractional cover (f) to specific, relatively small areas such as our test site. For the site, the RAL processor assigns class i=6 (broadleaf trees with groundcover) and $f=0.40 - 0.47$ (July – August). Particularly the value assigned to

f seems very low for the rice crops in summer. Taking the same class (i=6) and f=1 (full vegetation cover), the AATSR LST algorithm was applied to the brightness temperatures of the test site. The resulting LSTs (not shown in Table 5) agreed much better with the ground LSTs: the average overestimation was reduced to 1.4 °C, with a standard deviation of 0.5 °C and differences within the ± 2.5 °C limits specified for the LST product for all the days of the comparison.

The best results for the AATSR LST algorithm were obtained for class i=8 (broadleaf shrubs with groundcover) with f=1, which is appropriate for the fully developed rice crops in summer. Using the corresponding split-window coefficients in Eq. (4), the AATSR LST equation locally tuned to our study area is,

$$\text{LST} = 0.4[\sec(\theta)-1]pw + 1.5662 + 3.1384(T_{11n}-T_{12n})^n + 0.8965T_{12n} \quad (5)$$

with LST, T_{11n} and T_{12n} in °C. The precipitable water was taken $pw=2.5$ cm for midlatitudes in summer (as quoted before, the impact of pw on LST is small for the SW approach). Applying Eq. (5) to the AATSR brightness temperatures for the test area, we obtained the LSTs shown in the fifth column of Table 5, together with the differences with the ground LSTs (column 8). Differences ranged between -1.1 and 1.0 °C for all the days of the database, the average difference was -0.1 °C and the standard deviation was 0.5 °C.

3.3. Quadratic, emissivity dependent algorithm

The LST split-window algorithm of *Coll and Caselles* [1997] has a quadratic dependence on the brightness temperature difference and an explicit dependence on surface emissivity. For two generic channels at $11 \mu\text{m}$ and $12 \mu\text{m}$, channels 1 and 2 respectively, and using the mean emissivity, $\epsilon=(\epsilon_1+\epsilon_2)/2$, and the channel emissivity difference, $\Delta\epsilon=\epsilon_1-\epsilon_2$, the algorithm can be written as

$$\text{LST} = T_1 + a_0 + a_1(T_1-T_2) + a_2(T_1-T_2)^2 + \alpha(1-\epsilon) - \beta\Delta\epsilon \quad (6)$$

where coefficients a_0 , a_1 , a_2 , α and β depend on the particular split-window channels used, coefficients α and β depending also on the precipitable water and the brightness temperatures. This algorithm was applied and validated with NOAA/AVHRR data by *Coll and Caselles* [1997] and with GMS-5 VISSR data by *Prata and Cechet* [1999]. The quadratic dependence on the brightness temperature difference (T_1-T_2) accounts for the increase of the atmospheric correction for large amounts of atmospheric water vapor.

The algorithm coefficients for AATSR were calculated from a regression analysis over a database of simulated top-of-the-atmosphere AATSR radiances. The simulation database included 180 atmospheric radiosonde profiles obtained from land locations covering global conditions; with precipitable water ranging from 0 to 6 cm. Radiative transfer calculations were made with the MODTRAN4 code [Berk *et al.*, 1999] for a variety of surface temperatures and observation angles close to nadir (0° – 23°). The α and β coefficients were obtained according to Coll and Caselles [1997] for pw=2.5 cm, yielding $\alpha \approx 45$ K and $\beta \approx 55$ K for all the days of the comparison. Therefore, the algorithm can be written as

$$\text{LST} = T_{11n} + 0.04 + 0.94(T_{11n} - T_{12n}) + 0.25(T_{11n} - T_{12n})^2 + 45(1 - \epsilon) - 55\Delta\epsilon \quad (7)$$

The emissivity values necessary for the application of the algorithm were obtained from the ground measurements shown in Table 1 for mid-July, assuming that CE 312 channels 3 and 2 are similar to AATSR channels at 11 and 12 μm , respectively. Thus, $\epsilon = 0.983$ and $\Delta\epsilon = 0.005$ were taken. The LST values derived for the test site with Eq. (7) applied to AATSR data are shown in the sixth column of Table 5. The differences with the ground data (column 9) ranged from -1.0 to 1.0 $^\circ\text{C}$ for all the days of the comparison, with average difference of 0.0 $^\circ\text{C}$ and standard deviation of 0.5 $^\circ\text{C}$. The algorithm has little sensitivity to the precipitable water: for a pw increase (decrease) of 1 cm, the LST decreased (increased) by less than 0.1 $^\circ\text{C}$. With regard to the surface emissivity, uncertainties of ± 0.005 in both ϵ_{11n} and ϵ_{12n} , resulted in a LST uncertainty of ± 0.4 $^\circ\text{C}$.

4. VALIDATION OF DUAL ANGLE CORRECTION METHODS

The concept of the DA correction method is similar to the SW technique. In the DA method, the atmospheric differential absorption is obtained through the brightness temperature in the 11 μm channel, forward view, T_{11f} , instead of T_{12n} . In analogy with Section 3, we show first a linear regression analysis between the ground LSTs and the AATSR brightness temperatures in the nadir and forward view. Then, several DA algorithms for AATSR are validated with the ground LSTs.

4.1. Linear regression analysis

Similarly to Eq. (2), the simplest form of the DA algorithm could be written as

$$\text{LST} = T_{11n} + A_{\text{DA}}(T_{11n} - T_{11f}) + B_{\text{DA}} \quad (8)$$

where the 11 μm channel at the two views is selected, and A_{DA} and B_{DA} are the DA coefficients, which can be regarded as constants for the test site and during the time of the field campaigns. Using the ground LSTs and the concurrent AATSR brightness temperatures, T_{11n} and T_{11f} , Fig. (6) shows a plot of $LST - T_{11n}$ against $T_{11n} - T_{11f}$, for which the linear regression yielded coefficients A_{DA} and B_{DA} , with coefficient of determination $R^2=0.40$ and error of estimate for LST of $0.96\text{ }^\circ\text{C}$. These results were significantly worse than for the SW method in section 3.1 ($R^2=0.82$ and error of estimate of $0.52\text{ }^\circ\text{C}$). We can also use the unconstrained linear regression for the DA method,

$$LST = a'T_{11n} + b'T_{11f} + c' \quad (9)$$

for which $R^2=0.57$ and the error of estimate for LST is $0.75\text{ }^\circ\text{C}$, that improved the results obtained from Eq. (8) but still were less accurate than the corresponding results for the SW regression analysis (Eq. 3, Section 3.1). Finally, we also checked the DA technique with the 12 μm channel; that is, using Eq. (9) with T_{12n} and T_{12f} , instead of T_{11n} and T_{11f} . As expected, results were poorer than for the 11 μm channel: $R^2=0.49$ and error of estimate for LST of $0.82\text{ }^\circ\text{C}$.

4.2. Quadratic, emissivity dependent algorithms

There are few DA algorithms for LST retrieval published in the literature. We can cite the algorithms developed by *Sòria et al.* [2002] for AATSR and by *Sobrino et al.* [2004] for the Along Track Scanning Radiometer-2 (AATSR-2), the AATSR predecessor. Such algorithms were obtained from simulation of top-of-the-atmosphere brightness temperatures, being quadratic in the brightness temperature difference, $T_{11n} - T_{11f}$, and depending explicitly on the precipitable water, pw , and the surface emissivity in both views, ϵ_{11n} and ϵ_{11f} . The algorithm proposed by *Sòria et al.* [2002] for AATSR is

$$LST = T_{11n} + (2.67 - 0.07pw)(T_{11n} - T_{11f}) - (0.29 - 0.09pw)(T_{11n} - T_{11f})^2 - (0.31 + 0.28pw) + \\ + (72.5 - 7.9pw)(1 - \epsilon_{11n}) - (35.8 - 4.1pw)\Delta\epsilon \quad (10)$$

with $\Delta\epsilon = \epsilon_{11n} - \epsilon_{11f}$. An alternative algorithm can be obtained by adapting the SW method of *Coll and Caselles* [1997], Eq. (6), to the DA configuration. This implies simply taking channel 1 as the 11 μm channel at nadir view and channel 2 as the 11 μm channel at forward view. For the calculation of the coefficients we used the same simulation database as in Section 3.3, including the top-of-the-atmosphere brightness temperatures for the forward view. Then, the DA algorithm can be written as

$$LST = T_{11n} - 0.10 + 1.37(T_{11n} - T_{11f}) + 0.136(T_{11n} - T_{11f})^2 + 38(1 - \epsilon) - 67\Delta\epsilon \quad (11)$$

with $\epsilon = (\epsilon_{11n} + \epsilon_{11f})/2$ and $\Delta\epsilon = \epsilon_{11n} - \epsilon_{11f}$. The coefficients for the emissivity terms ($\alpha = 38$ K and $\beta = 67$ K) were calculated for an atmospheric precipitable water of 2.5 cm.

In order to apply the DA algorithms of Eqs. (10) and (11), the surface emissivities must be known at the two observation angles. According to the measurements of Table 1, we can take $\epsilon_{11n} = 0.985$ for the rice crops. There were not available measurements for the emissivity of the rice crops in the forward view, ϵ_{11f} , although $\Delta\epsilon > 0$ is generally assumed. However, it might be expected that the angular emissivity difference was small in this case. *Lagouarde et al.* [1995] performed angular measurements of brightness temperatures for several surfaces. For full cover alfalfa crops, the differences between the nadir and off-nadir (60°) brightness temperatures were within 0.5 °C. Such small variation was attributed to the high density of the canopy and the absence of water stress (as for the rice crops in summer), which are likely to reduce the angular effects. A temperature decrease of 0.5 °C between nadir and off-nadir observations is approximately equivalent to an emissivity decrease of 0.01 between both viewing conditions.

Thus, taking $\epsilon_{11n} = 0.985$ and $\epsilon_{11f} = 0.975$, Eqs. (10) and (11) were applied to the AATSR data and the LSTs were obtained for the test site as shown in Table 6. The differences between the ground and the AATSR derived LSTs are also given in Table 6. According to these results, Eq. (10) overestimates the ground LST by 0.9 °C in average, with differences ranging from -3.1 to 0.5 °C. Eq. (11) yields a negligible average bias (0.0 °C), with differences between -2.0 and 2.4 °C. For both algorithms, the standard deviation of the differences was about 1 °C. The two DA algorithms showed different sensitivity to the angular emissivity difference. If $\Delta\epsilon$ is increased by 0.01, the retrieved LSTs decrease by 0.25 °C for Eq. (10) and by 0.5 °C for Eq. (11). The sensitivity of the algorithms to the precipitable water, pw, was also checked. A change of 1 cm in pw yielded variations in LST smaller than 0.3 °C for Eq. (10) and smaller than 0.1 °C for Eq. (11).

5. CONCLUSIONS

Ground measurements concurrent to AATSR observations were used to validate LSTs derived with SW and DA algorithms in a homogeneous test site close to Valencia, Spain. The results shown in this study stress the need for a good specification of the SW coefficients for LST retrieval, based either on land cover classification and vegetation cover fraction estimates, or with the surface emissivity. In this case (Eqs. (5) and (7)), the SW

technique can provide the LST with good accuracy: differences with the ground data in the ± 1 °C range for all the data of the comparison, nearly zero average bias and standard deviations of 0.5 °C. However, the $0.5^\circ \times 0.5^\circ$ longitude/latitude resolution used by the current AATSR LST operational algorithm to assign values for land class (i) and vegetation cover fraction (f) are too much coarse to account for the large heterogeneity of land surfaces. It was shown that this coarseness leads to large LST errors in particular areas, as shown for the Valencia test site. Therefore, a much finer spatial resolution should be used for i and f in the operational LST processor (ideally, the same as for the LST product, i. e., 1 km^2). These results confirm the conclusions shown by *Coll et al.* [2005] for a more limited data set.

The performance of the DA algorithms appeared lower than of the SW algorithms, showing larger differences with the ground LSTs (standard deviations of 1 °C). It was also noted in the regression analysis, which showed smaller correlations of LST with T_{11n} and T_{11f} and larger errors of estimate for LST. The lower accuracy of the DA method is due to the directional effects in radiometric temperatures expected for rough, non-isothermal land surfaces, and to uncertainties in the angular variation of land surface emissivity. The Valencia test site can be regarded as an ideal case for DA LST validation, taking into account its thermal homogeneity at the AATSR spatial scale, and that the full-cover, well irrigated rice crops are expected to show only small directional effects in the brightness temperatures. For this reason, we consider that larger LST estimation errors may be expected for DA algorithms in other types of land surfaces.

ACKNOWLEDGMENTS

This work was financed by the *Ministerio de Ciencia y Tecnología (Acción Especial REN2002-11605-E/CLI; Project REN2001-3116/CLI, and “Ramón y Cajal” Research Contract of Dr. E. Valor)*, the *Ministerio de Educación y Ciencia (Project CGL2004-06099-C03-01, co-financed with European Union FEDER funds, Acción Complementaria CGL2004-0166-E and Research Contract of Dr. R. Nicolòs)*, and the University of Valencia (*V Segles Research Grant of Mr. J. M. Sánchez*). We thank the AATSR Validation Team, University of Leicester, and the European Space Agency (under CAT-1 project 3466) for providing the AATSR data.

REFERENCES

- Becker, F. and Z.-L. Li (1990), Towards a local split-window method over land surfaces, *International Journal of Remote Sensing*, 11, 369-394.
- Berk, A., G.P. Anderson, P.K. Acharya, J. H. Chetwynd, L. S. Bernstein, E.P. Shettle, M.W. Matthew, and S.M. Adler-Golden (1999), MODTRAN4 user's manual, Air Force Research Laboratory, Space Vehicles Directorate, Air Force Materiel Command, Hascom AFB, MA, USA.
- Caselles, V., C. Coll, E. Valor, and E. Rubio (1997), Thermal band selection for the PRISM instrument. 2. Analysis and comparison of existing atmospheric and emissivity correction methods for land surface temperature recovery, *Journal of Geophysical Research*, 102D, 19611-19627.
- Coll, C. and V. Caselles (1997), A global split-window algorithm for land surface temperature from AVHRR data: Validation and algorithm comparison, *Journal of Geophysical Research*, 102D, 16697-16713.
- Coll, C., V. Caselles, J. M. Galve, E. Valor, R. Niclòs, J. M. Sánchez and R. Rivas (2005), Ground measurements for the validation of land surface temperatures derived from AATSR and MODIS data, *Remote Sensing of Environment*, 97, 288-300.
- Deschamps, P. Y., and T. Phulpin (1980), Atmospheric correction of infrared measurements of sea surface temperature using channels at 3.7, 11 and 12 μm , *Boundary-Layer Meteorology*, 18, 131-143.
- Lagouarde, J. P., Y. H. Kerr and Y. Brunet (1995), An experimental study of angular effects on surface temperature for various plant canopies and bare soils, *Agricultural and Forest Meteorology*, 77, 167-190.
- Llewellyn-Jones, D., M. C. Edwards, C. T. Mutlow, A. R. Birks, I. J. Barton and H. Tait, (2001), AATSR: Global-change and Surface-Temperature measurements from ENVISAT, *ESA Bulletin*, February 2001, 11-21.
- McMillin, L. M. (1975), Estimation of sea surface temperatures from two infrared window measurements with different absorption, *Journal of Geophysical Research*, 80, 5113-5117.
- Prabhakara, C., G. Dalu, and V. G. Kunde (1974), Estimation of sea surface temperature from remote sensing in the 11- to 13- μm window region, *Journal of Geophysical Research*, 79, 5039-5044.
- Prata, A. J. (1994), Land surface temperatures derived from the Advanced Very High Resolution Radiometer and the Along Track Scanning Radiometer. II. Experimental results and validation of AVHRR algorithms., *Journal of Geophysical Research*, 99D, 13025-13058.
- Prata, A. J. (2000), Land surface temperature measurement from space: AATSR Algorithm Theoretical Basis Document, *Technical Report*, 27 pp., CSIRO Atmospheric Research, Aspendale, Australia.

- Prata, A. J. and R. P. Cechet (1999), An assessment of the accuracy of land surface temperature determination from the GMS-5 VISSR, *Remote Sensing of Environment*, 67, 1-14.
- Rubio, E., V. Caselles, C. Coll, E. Valor and F. Sospedra (2003), Thermal-infrared emissivities of natural surfaces: Improvements on the experimental set-up and new measurements, *International Journal of Remote Sensing*, 24, 5379-5390.
- Salisbury, J. W. and D. M. D'Aria (1992), Emissivity of terrestrial materials in the 8-14 μm atmospheric window, *Remote Sensing of Environment*, 42, 83-106.
- Saunders, P. M. (1970), Corrections for airborne radiation thermometry, *Journal of Geophysical Research*, 75, 7596-7601.
- Sobrino, J. A., G. Sòria and A. J. Prata (2004), Surface temperature retrieval from Along Track Scanning Radiometer 2 data: Algorithms and validation, *Journal of Geophysical Research*, 109, D11101, doi: 10.1029/2003JD004212.
- Sòria, G., J. A. Sobrino, J. Cuenca, A. J. Prata, J. C. Jiménez-Muñoz, M. Gómez and J. El-Kharraz (2002), Surface temperature retrieval from AATSR data: multichannel and multiangle algorithms, First Symposium on Recent Advances in Quantitative Remote Sensing, University of Valencia, Torrent, Spain.
- Wan, Z. and J. Dozier (1996), A generalized split-window algorithm for retrieving land surface temperature from space, *IEEE Transactions on Geoscience and Remote Sensing*, 34, 892-905.
- Wan, Z., Y. Zhang, Q. Zhang and Z.-L. Li (2002), Validation of the land-surface temperature products retrieved from Terra Moderate Resolution Imaging Spectroradiometer data, *Remote Sensing of Environment*, 83, 163-180.
- Yamaguchi, Y., A. B. Kahle, H. Tsu, T. Kawakami and M. Pniel (1998), Overview of Advanced Spaceborne Thermal Emission and Reflection Radiometer (ASTER), *IEEE Transactions on Geoscience and Remote Sensing*, 36, 1062-1071.

TABLES

Table 1. Emissivity values for the rice crop measured with the four channels of the CE 312 instrument.

Date	Ch. 4 (8.2-9.2 μm)	Ch. 3 (10.5-11.5 μm)	Ch. 2 (11.5-12.5 μm)	Ch. 1 (8-13 μm)
July 15	0.985 \pm 0.004	0.985 \pm 0.002	0.980 \pm 0.005	0.983 \pm 0.003
September 5	0.982 \pm 0.004	0.983 \pm 0.002	0.977 \pm 0.005	0.980 \pm 0.003

Table 2.- List of dates and AATSR overpasses time with concurrent ground temperature measurements. Columns 4-7 give the temperature and uncertainty corresponding to each radiometer/transect. The last column gives the average LST and uncertainty to be compared with AATSR data.

Year	Date (day/month)	Overpass time(UTC)	LST \pm σ (T) ($^{\circ}\text{C}$)				
			CE1	CE2	Everest	AGA	Average
2002	10/07	10:30	28.4 \pm 0.6	–	29.1 \pm 1.0	–	28.6 \pm 0.6
	13/07	10:37	27.2 \pm 0.8	–	28.2 \pm 0.8	27.9 \pm 1.0	27.6 \pm 0.9
	26/07	10:28	27.8 \pm 0.5	–	28.2 \pm 0.8	28.1 \pm 0.9	27.9 \pm 0.6
	08/08	10:19	26.4 \pm 0.6	–	–	26.7 \pm 1.0	26.5 \pm 0.7
	14/08	10:31	28.4 \pm 0.5	–	28.6 \pm 0.8	–	28.5 \pm 0.5
	17/08	10:37	29.0 \pm 0.6	–	29.3 \pm 0.7	–	29.1 \pm 0.6
	05/09	10:40	28.0 \pm 0.8	–	–	–	28.0 \pm 0.8
2003	08/07	10:23	28.4 \pm 0.8	28.4 \pm 0.7	28.6 \pm 0.9	27.8 \pm 0.9	28.3 \pm 0.7
	11/07	10:28	29.2 \pm 0.8	29.1 \pm 0.5	28.9 \pm 0.8	–	29.1 \pm 0.7
	14/07	10:34	28.7 \pm 0.8	28.6 \pm 0.4	28.4 \pm 0.8	–	28.6 \pm 0.6
	24/07	10:20	28.5 \pm 0.6	29.1 \pm 0.4	28.9 \pm 0.9	–	28.8 \pm 0.6
	30/07	10:30	29.2 \pm 0.3	29.4 \pm 0.4	28.4 \pm 0.5	–	28.9 \pm 0.6
	12/08	10:23	31.6 \pm 0.5	31.0 \pm 0.5	31.1 \pm 0.8	–	31.3 \pm 0.6
2004	28/06	10:34	29.1 \pm 0.6	29.3 \pm 0.6	–	–	29.2 \pm 0.6
	08/07	10:20	25.7 \pm 0.6	–	25.8 \pm 0.7	–	25.7 \pm 0.6
	14/07	10:31	27.4 \pm 0.5	26.9 \pm 0.6	27.6 \pm 0.9	–	27.2 \pm 0.7
	27/07	10:23	27.6 \pm 0.5	27.8 \pm 0.4	–	–	27.7 \pm 0.4
	30/07	10:28	27.5 \pm 0.5	28.0 \pm 0.58	–	–	27.8 \pm 0.4
	12/08	10:20	28.6 \pm 0.6	28.1 \pm 0.5	28.6 \pm 0.7	–	28.4 \pm 0.6
2005	12//07	10:23	26.8 \pm 0.7	27.3 \pm 0.3	–	–	27.0 \pm 0.6
	21/07	10:39	28.2 \pm 0.5	28.8 \pm 0.5	–	–	28.5 \pm 0.6
	28/07	10:20	28.5 \pm 0.5	29.1 \pm 0.4	28.5 \pm 0.5	–	28.8 \pm 0.5
	06/08	10:37	28.3 \pm 0.3	27.8 \pm 0.5	–	–	28.0 \pm 0.5

Table 3. Average brightness temperatures for the 3×3 pixels closest to the test site center, for the 11 and 12 μm channels, nadir view. The standard deviation of temperatures, σ , and the satellite viewing angle are also given.

Year	Date (day/month)	Nadir view				
		Viewing angle (°)	T _{11n} (°C)	σ (T _{11n}) (°C)	T _{12n} (°C)	σ (T _{12n}) (°C)
2002	10/07	3.7	25.04	0.09	22.99	0.14
	13/07	13.8	22.28	0.08	19.26	0.08
	26/07	1.11	23.39	0.10	20.68	0.10
	08/08	16.2	20.29	0.08	17.31	0.09
	14/08	3.9	23.69	0.12	21.52	0.07
	17/08	13.91	22.81	0.09	19.84	0.08
2003	05/09	19.06	24.10	0.10	22.03	0.10
	08/07	11.13	25.30	0.12	23.03	0.10
	11/07	1.20	27.03	0.13	25.50	0.12
	14/07	8.66	24.73	0.15	22.39	0.13
	24/07	16.25	24.68	0.15	22.36	0.11
	30/07	3.74	23.44	0.11	20.63	0.06
2004	12/08	11.13	28.10	0.10	26.51	0.11
	28/06	8.66	26.41	0.10	24.36	0.10
	08/07	16.33	23.15	0.41	21.60	0.37
	14/07	3.74	22.45	0.12	19.78	0.18
	27/07	11.05	25.02	0.11	23.35	0.09
	30/07	1.19	23.37	0.12	20.58	0.08
2005	12/08	16.25	25.50	0.12	23.98	0.15
	12//07	11.13	24.64	0.07	23.04	0.06
	21/07	18.97	25.40	0.08	23.63	0.07
	28/07	16.33	24.75	0.09	22.67	0.11
	06/08	13.66	25.35	0.06	23.68	0.06

Table 4. Average brightness temperatures for the four pixels closest to the test site center, for the 11 and 12 μm channels, forward view. The standard deviation of temperatures, σ , and the satellite viewing angle are also given.

Year	Date (day/month)	Forward view				
		Viewing angle ($^{\circ}$)	T_{11f} ($^{\circ}\text{C}$)	$\sigma(T_{11f})$ ($^{\circ}\text{C}$)	T_{12f} ($^{\circ}\text{C}$)	$\sigma(T_{12f})$ ($^{\circ}\text{C}$)
2002	10/07	55.17	22.66	0.14	20.10	0.16
	13/07	54.20	19.13	0.09	15.68	0.08
	26/07	55.22	20.81	0.04	17.69	0.04
	08/08	53.87	17.43	0.09	13.97	0.07
	14/08	55.16	21.18	0.06	18.56	0.05
	17/08	54.22	20.49	0.09	16.93	0.09
	05/09	53.25	22.86	0.09	20.19	0.10
2003	08/07	54.60	22.93	0.06	20.15	0.08
	11/07	55.22	25.15	0.05	23.38	0.04
	14/07	54.84	22.23	0.09	19.58	0.07
	24/07	53.86	22.46	0.41	19.86	0.40
	30/07	55.17	20.30	0.01	17.08	0.01
	12/08	54.60	26.71	0.07	24.65	0.09
2004	28/06	54.84	23.51	0.07	21.27	0.08
	08/07	53.85	21.46	0.17	19.50	0.19
	14/07	55.16	19.83	0.09	16.69	0.03
	27/07	54.61	23.08	0.02	21.14	0.01
	30/07	55.23	20.43	0.04	16.93	0.05
	12/08	53.86	24.24	0.14	22.27	0.17
2005	12//07	54.58	22.97	0.14	21.00	0.10
	21/07	53.27	23.65	0.09	21.59	0.08
	28/07	53.81	22.31	0.04	19.91	0.04
	06/08	54.27	23.98	0.06	21.91	0.05

Table 5. Comparison of ground and AATSR LSTs derived with SW algorithms: the RAL processor, Eq. (5), and Eq. (7). The last three columns show the difference between the ground and the AATSR LST for each algorithm.

Year	Date (day/month)	Ground LST (°C)	AATSR LST (°C)			Ground – AATSR LST (°C)		
			RAL	Eq. (5)	Eq. (7)	RAL	Eq. (5)	Eq. (7)
2002	10/07	28.6	32.1	28.6	28.6	-3.5	0.0	0.0
	13/07	27.6	31.8	28.3	28.0	-4.2	-0.7	-0.4
	26/07	27.9	32.0	28.6	28.3	-4.1	-0.7	-0.4
	08/08	26.5	29.4	26.5	25.9	-2.9	0.0	0.6
	14/08	28.5	30.8	27.7	27.5	-2.3	0.8	1.0
	17/08	29.1	32.0	28.7	28.4	-2.9	0.4	0.7
	05/09	28.0	31.2	27.9	27.7	-3.2	0.1	0.3
2003	08/07	28.3	33.1	29.4	29.3	-4.8	-1.1	-1.0
	11/07	29.1	33.0	29.2	29.6	-3.9	-0.1	-0.5
	14/07	28.6	32.7	29.0	28.9	-4.1	-0.4	-0.3
	24/07	28.8	32.5	28.9	28.8	-3.7	-0.1	0.0
	30/07	28.9	32.5	28.9	28.6	-3.6	0.0	0.3
	12/08	31.3	33.9	30.3	30.8	-2.6	1.0	0.5
2004	28/06	29.2	34.0	29.8	30.0	-4.8	-0.6	-0.8
	08/07	25.7	28.8	25.8	25.8	-3.1	-0.1	-0.1
	14/07	27.2	31.1	27.7	27.3	-3.9	-0.5	-0.1
	27/07	27.7	31.2	27.8	27.8	-3.5	-0.1	-0.1
	30/07	27.8	32.1	28.8	28.5	-4.3	-1.0	-0.7
	12/08	28.4	31.0	27.9	28.1	-2.6	0.5	0.3
2005	12//07	27.0	30.6	27.1	27.3	-3.6	-0.1	-0.3
	21/07	28.5	31.8	28.4	28.4	-3.3	0.1	0.1
	28/07	28.8	32.0	28.5	28.4	-3.2	0.3	0.4
	06/08	28.0	31.0	28.1	28.2	-3.0	-0.1	-0.2
Average difference (°C)						-3.5	-0.1	0.0
Standard deviation (°C)						0.7	0.5	0.5

Table 6. Comparison of ground LSTs with AATSR LSTs derived with DA algorithms: Eq. (10), and Eq. (11).

The last two columns show the difference between the ground LST and the AATSR LST for each algorithm.

Year	Date (day/month)	Ground LST (°C)	AATSR LST (°C)		Ground – AATSR LST (°C)	
			Eq. (10)	Eq. (11)	Eq. (10)	Eq. (11)
2002	10/07	28.6	30.0	28.9	-1.4	-0.3
	13/07	27.6	29.0	27.9	-1.4	-0.3
	26/07	27.9	28.9	27.8	-1.0	0.1
	08/08	26.5	26.5	25.4	0.0	1.1
	14/08	28.5	29.0	27.9	-0.5	0.6
	17/08	29.1	27.8	26.7	1.3	2.4
	05/09	28.0	26.6	26.0	1.4	2.0
2003	08/07	28.3	30.2	29.1	-1.9	-0.8
	11/07	29.1	31.1	30.1	-2.0	-1.0
	14/07	28.6	30.0	28.9	-1.4	-0.3
	24/07	28.8	31.3	30.2	-2.5	-1.4
	30/07	28.9	30.2	29.1	-1.3	-0.2
	12/08	31.3	30.8	30.1	0.5	1.2
2004	28/06	29.2	32.3	31.2	-3.1	-2.0
	08/07	25.7	27.1	26.1	-1.4	-0.4
	14/07	27.2	28.2	27.1	-1.0	0.1
	27/07	27.7	29.1	28.2	-1.4	-0.5
	30/07	27.8	29.8	28.6	-2.0	-0.8
	12/08	28.4	27.9	27.3	0.5	1.1
2005	12//07	27.0	28.2	27.3	-1.2	-0.3
	21/07	28.5	29.1	28.2	-0.6	0.3
	28/07	28.8	30.0	28.9	-1.2	-0.1
	06/08	28.0	28.2	27.5	-0.2	0.5
Average difference (°C)					-0.9	0.0
Standard deviation (°C)					1.1	1.0

FIGURES

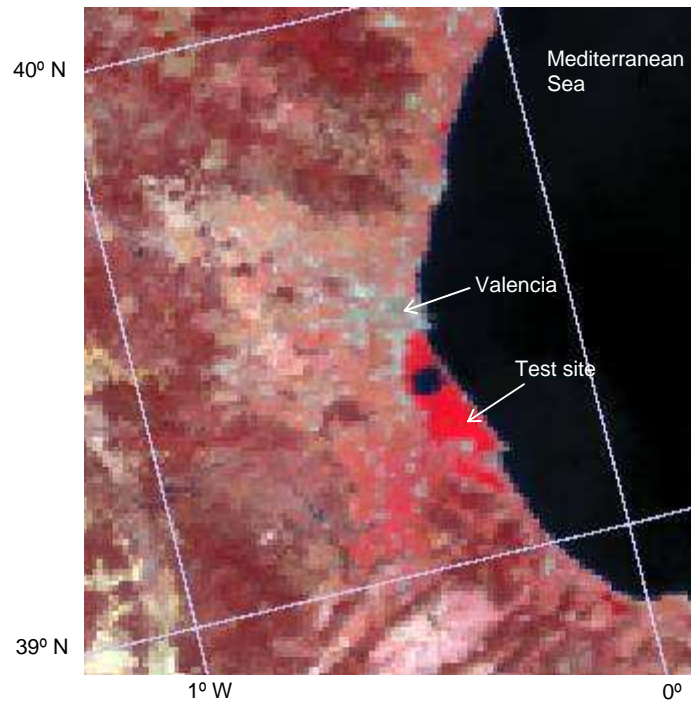


Figure 1. AATSR color composite showing the location of the Valencia test site, on July 11, 2003. The rice field area is shown in red. The RGB components are channels at 0.87 μm , 0.66 μm and 0.55 μm , nadir view, respectively.

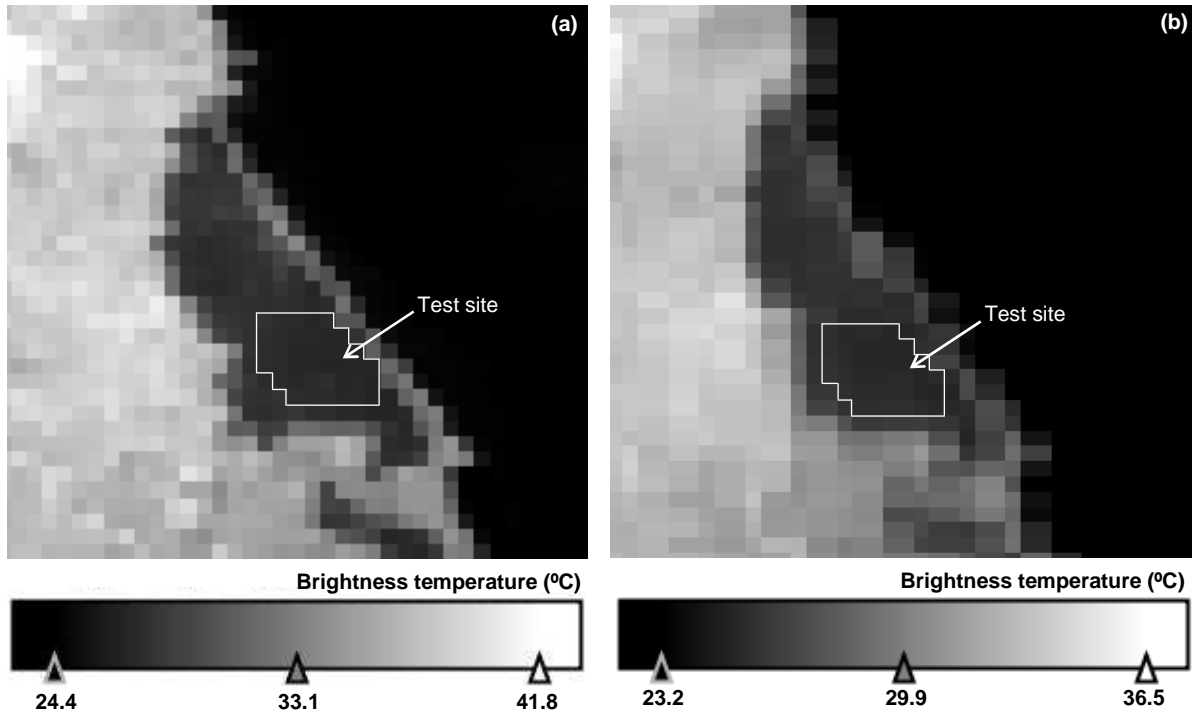


Figure 2. Brightness temperature image of the rice field area, AATSR channel at 11 μm , on July 11, 2003. (a) nadir view, and (b) forward view. The location of the test site is indicated. Part of the rice field area is enclosed by a solid-line polygon.

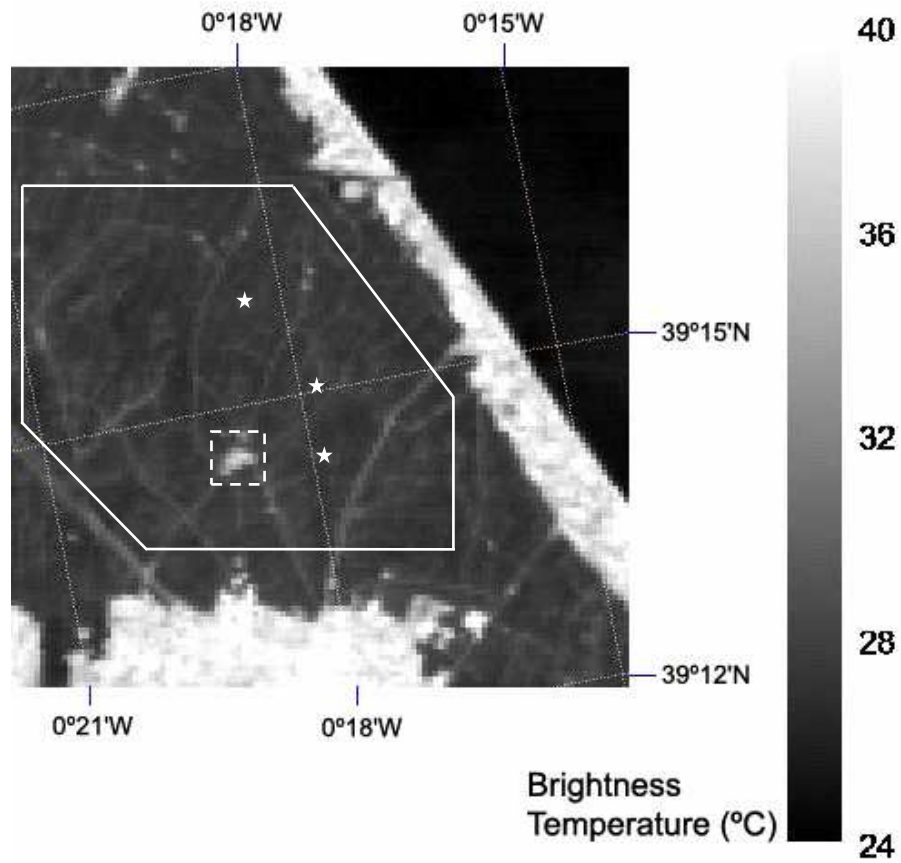


Figure 3. Brightness temperature image ($10 \times 10 \text{ km}^2$) from ASTER band 13 ($10.66 \text{ }\mu\text{m}$), on August 3, 2004. The center of the three test sites is indicated with stars. The solid-line polygon encloses part of the rice field area. The dashed-line square encloses the largest thermal hot spot in the area.

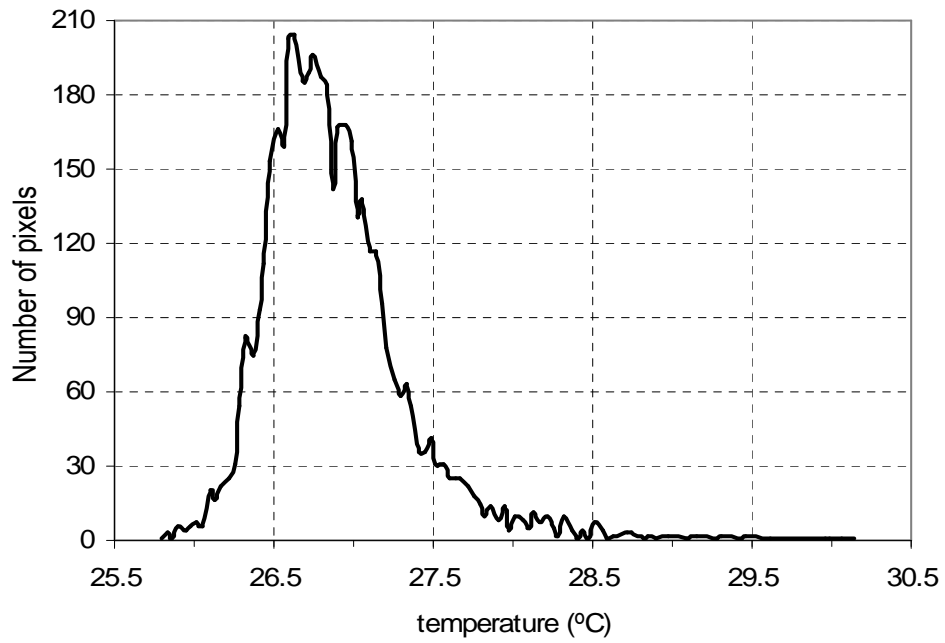


Figure 4. Histogram of brightness temperatures for the pixels inside the solid-line polygon of Figure 3, excluding the pixels of the dashed-line square.

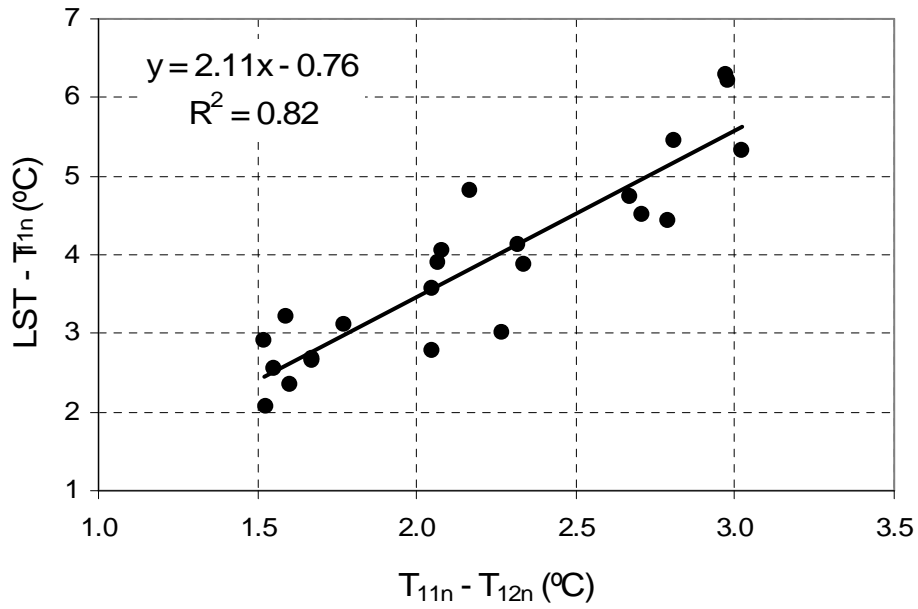


Figure 5. Linear regression analysis of $\text{LST} - T_{11n}$ against the brightness temperature difference $T_{11n} - T_{12n}$ for the experimental data of the test site. The linear equation and the coefficient of determination (R^2) are shown.

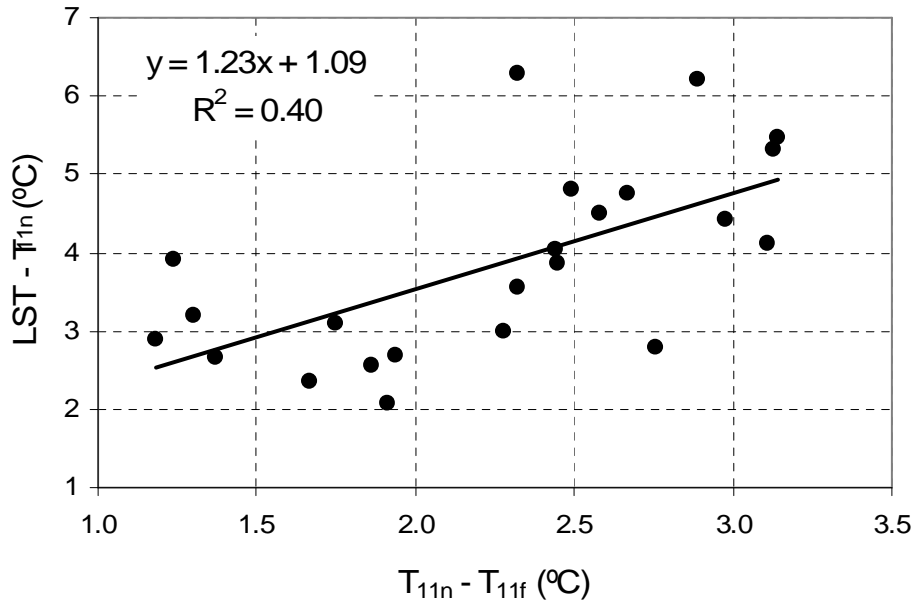


Figure 6. Linear regression analysis of $LST - T_{11n}$ against the brightness temperature difference $T_{11n} - T_{11f}$ for the experimental data of the test site. The linear equation and the coefficient of determination (R^2) are shown.